THE JOURNAL OF PHYSICAL CHEMISTRY C

Article

pubs.acs.org/JPCC

Curvature Effects on the Interfacial Capacitance of Carbon Nanotubes in an Ionic Liquid

Eunsu Paek,[†] Alexander J. Pak,[†] and Gyeong S. Hwang*

Department of Chemical Engineering, University of Texas, Austin, Texas 78712, United States

Supporting Information

ABSTRACT: Carbon nanotube (CNT) electrodes in supercapacitors have recently demonstrated enhanced performance compared to conventional carbon-based electrodes; however, the underlying relationships between electrode curvature and capacitance remain unclear. Using computer simulations, we evaluate the capacitive performance of metallic (6,6), (10,10), and (16,16) CNTs in [BMIM][PF_6] ionic liquid (IL), with particular attention to the relative contributions of the electric double layer (EDL) capacitance (C_D) at the CNT/IL interface and the electrode quantum capacitance (C_Q). Our classical molecular dynamics simulations reveal that C_D improves with increasing electrode curvature, which we discuss in terms of how the curvature affects both the electric field strength and EDL microstructure. In addition, the C_Q of the CNTs is constant near the Fermi level and increases with curvature, as also demonstrated by density functional theory calculations. Our study shows that the electrode curvature effect on the total interfacial capacitance can be a strong function of applied voltage, which we attribute to the shifting contributions of C_Q and C_D.

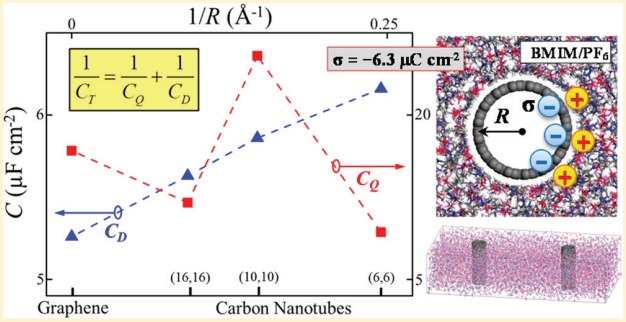

I. INTRODUCTION

Electrical double-layer capacitors (EDLCs), or supercapacitors, are electrochemical energy storage devices that electrostatically store charge at the electrode−electrolyte interface. These devices have advantageous power densities and lifetimes compared to other energy storage devices such as batteries.[1,2] Recently, carbon-based materials (such as activated carbon and graphene) have shown considerable potential as supercapacitor electrodes due to their high specific surface area and good electrical conductivity.[1,3−7] In addition, room-temperature ionic liquids[8,9] (RTILs), "solvent-free" ions that are in the liquid state, have attracted much interest as an electrolyte due to their wide electrochemical windows, high chemical and thermal stability, extremely low volatility, and nonflammability. EDLCs, however, suffer from poor energy density, which has motivated research into improving the capacitance of these devices.[7−17]

After Ijima's seminal paper[18] in 1991, interest in carbon nanotubes (CNTs) has grown tremendously for a variety of applications, including field-effect transistors, chemical sensors, energy conversion devices, and energy storage devices.[19,20] In particular, the incorporation of CNT-based electrodes in EDLCs have demonstrated superior performance compared to conventional activated carbon electrodes.[21−25] Recent experimental work by Honda and co-workers has demonstrated that the electrode topology, specifically different CNT curvatures, can significantly impact the EDLC capacitance.[22] While these studies can begin to elucidate the behavior of EDLCs with various electrode topologies, our understanding of the phenomena at the electrode−electrolyte interface is still limited due largely to difficulties in experimental characterization at the molecular scale.

The majority of theoretical studies[26−28] have focused on how CNT pore sizes influence the double layer capacitance (C_D), yet few have investigated the role of the positive (or outer) CNT curvature. Huang and co-workers developed a model based on a classical geometric capacitor and suggested that C_D increases with decreasing CNT radius.[29] From classical molecular dynamics (MD) simulations, Feng and co-workers also showed that a (5,5) CNT electrode results in at least a 30% enhancement in capacitance compared to planar graphene electrodes with 1-butyl-3-methyl-imidazolium hexafluorophosphate ([BMIM][PF_6]) and [BMIM][Cl] ILs.[30] A recent study from the same group also predicted that the C_D increases nonlinearly with CNT curvature in [EMIM][TFSI] IL, with symmetric behavior at the anode and cathode due to the similarity in cation/anion size.[31] A detailed analysis of the impact of both different CNT curvatures and cation/anion asymmetry on the EDL microstructure and C_D, however, is still lacking.

Recent experimental[32,33] and theoretical[34,35] works have also indicated that the total interfacial capacitance (C_T) of low-dimensional carbon electrodes—of which CNTs should be included—strongly depends on the relative contributions of C_D and the electrode quantum capacitance (C_Q). In addition to C_D,

Received: August 13, 2013
Revised: October 8, 2013
Published: October 11, 2013

   dx.doi.org/10.1021/jp408085w | J. Phys. Chem. C 2013, 117, 23539−23546

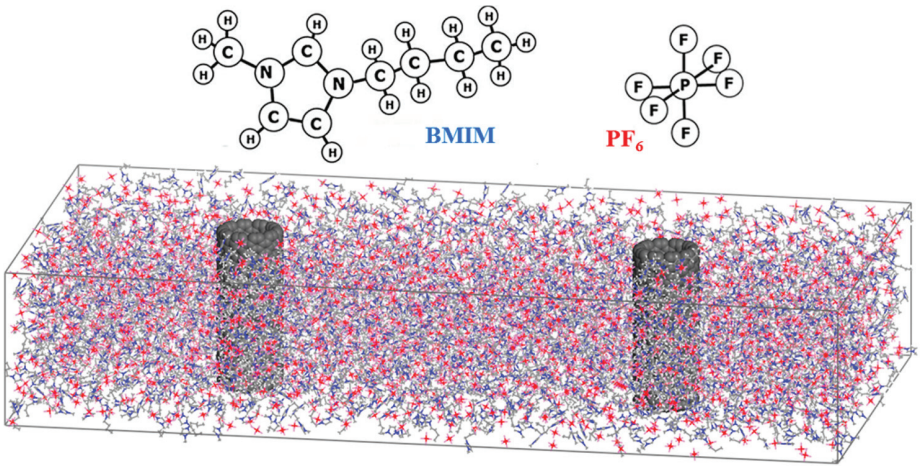

Figure 1. Schematic of BMIM, PF_6, and the simulation domain. Two CNTs of the same radius are placed in the simulation domain such that the IL maintains its bulk density in the middle and edges of the domain. White, blue, and gray lines indicate H, N, and C atoms in BMIM while red and pink lines indicate F and P atoms in PF_6, respectively. Periodic boundary conditions are applied in the *x*, *y*, and *z* directions.

the CNT curvature can also influence C_Q. Yet, the relative roles of both C_Q and C_D in CNT-based EDLCs have yet to be reported.

In this paper, we investigate the effect of electrode curvature on the interfacial capacitance. Specifically, we study three different metallic CNT [(6,6), (10,10), and (16,16)] electrodes in [BMIM][PF_6] IL using combined density functional theory (DFT) and classical MD simulations. Our analysis is particularly interested in understanding the relative contributions of C_D and C_Q as compared to pristine graphene electrodes. First, we investigate the microstructure of [BMIM][PF_6] near the CNT electrodes by varying the electrode surface charge density using MD simulations, and use the calculated IL distribution to evaluate the potential variation and EDL integral capacitance. Then, we employ DFT calculations to estimate the C_Q of the CNTs. Based on the calculation results, we discuss the impact of electrode curvature on the capacitive performance, especially the curvature effect on C_D and C_Q in terms of applied voltage.

II. METHODS

Classical Molecular Dynamics. We employed MD simulations with the OPLS-AA force field[36,37] to determine the microstructure of [BMIM][PF_6] near the (6,6), (10,10), (16,16) CNTs and graphene electrodes; details on the force field parameters can be found in ref 34. As illustrated in Figure 1, the CNT/IL simulation domain consists of [BMIM][PF_6] IL pairs surrounding two CNTs with periodic boundary conditions in all three directions; each CNT represents one positive and negative electrode to maintain charge neutrality. Additional details about the simulations (e.g., radius and length of the CNTs, size of the simulation domain, and number of ion pairs) are shown in the Table S1. Note that we set the domain large enough such that the electrolyte maintains bulk properties at the middle and edges of the domain. For $\sigma = \pm 6.3$ and ± 12.7 $\mu C/cm^2$, the C atoms of each CNT were assigned uniform atomic charges. The graphene/IL system consists of 312 [BMIM][PF_6] pairs between two graphene electrodes (34.18×34.53 $Å^2$) separated by 100 Å. For $\sigma = \pm 6.33$ and ± 12.67 $\mu C/cm^2$, the C atoms in graphene were also assigned uniform atomic charges.

We annealed and quenched each MD simulation initially at 1000 K for 0.5 ns followed by 0.5 ns at 300 K for two cycles, and then further equilibrated for 3 ns at 300 K using a time step of 1 fs. Production runs were carried out for 4 ns with atomic positions recorded every 5 ps. All runs were in the NVT ensemble with the target temperature controlled by a Nose–Hoover thermostat[38] with a 100 fs damping parameter. All MD simulations were performed with the Large-scale Atomic/Molecular Massively Parallel Simulator (LAMMPS) program.[39] MD results reported herein were obtained from the average of four independent simulations with different initial atomic configurations.

Density Functional Theory. The atomic and electronic structures of pristine graphene and each of the CNTs were calculated using DFT within the Perdew–Wang 91 generalized gradient approximation[40] (GGA-PW91), as implemented in the Vienna Ab initio Simulation Package[41] (VASP). We employed the projector augmented wave (PAW) method[42] to describe the interaction between core and valence electrons, and a planewave basis set with a kinetic energy cutoff of $E_{cut} = 400$ eV. The CNT structures were modeled using periodic boundary conditions in all three directions; each of the supercells contained 5 unit cells corresponding to 12.33 Å in length and a vacuum space of at least 12 Å (in the radial direction to avoid interactions with the periodic image). For the Brillouin zone integration, we used a $(1 \times 1 \times 12)$ Monkhorst-Pack[43] *k*-point mesh for geometry optimization and energy calculations and increased the number of *k*-points to ensure convergence for electronic structure calculations. Details on the calculations for pristine graphene can be found in ref 34.

III. RESULTS AND DISCUSSION

A. Effect of Curvature on EDL Microstructure. The integral EDL capacitance can be obtained from the relationship between excess surface charge density (σ) and potential drop within the EDL (ϕ_D); that is, $C_D = \sigma/(\phi_D - \phi_Z)$, where ϕ_Z is known as the potential of zero charge (PZC). To obtain C_D, we first evaluated the [BMIM][PF_6] IL microstructure near (6,6), (10,10), (16,16) CNTs and graphene using MD simulations, as described in the following section.

Figure 2 shows the mass density (ρ_m) profiles of cationic BMIM and anionic PF_6 near graphene (a,d), the (16,16) CNT

dx.doi.org/10.1021/jp408085w | J. Phys. Chem. C 2013, 117, 23539–23546

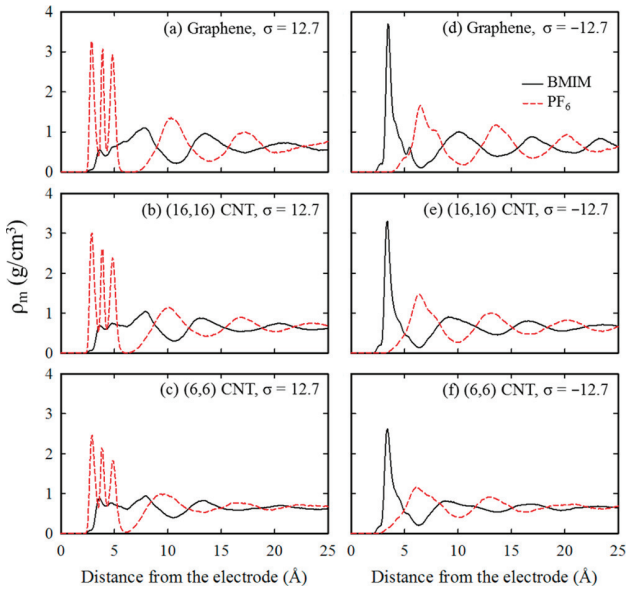

Figure 2. Calculated mass density (ρ_m) profiles for BMIM and PF_6 near graphene, (16,16) CNTs, and (6,6) CNTs at the listed σ (in $\mu C/cm^2$) as a function of distance from the electrode surface.

(b,e), and the (6,6) CNT (c,f) along the direction normal to the electrode surface with excess surface charge density $\sigma = \pm 12.7$ $\mu C/cm^2$ (for $\sigma = \pm 6.3$ $\mu C/cm^2$, refer to Figure S2, Supporting Information). Each profile exhibits alternating cation/anion layering that dampens away from the electrode, which tends to extend about 2−3 nm before showing bulk-like characteristics. This layering behavior is consistent with previous studies near planar[44−46] and cylindrical[30,31] surfaces. We also find that the orientations of IL ions at the interface show a similar behavior near the graphene and CNT electrodes; detailed analysis of the IL orientation near graphene can be found in ref 34. Near the positive electrodes (a−c), PF_6 exhibits three peaks which correspond to F, P, and F atoms, respectively; the electrostatic attraction between the positive electrode and the negatively charged F atoms causes these atoms to orient parallel (concentric in the CNT cases) to the electrode surface. Similarly, the BMIM peak near the negative electrode (d−f) indicates the tendency of the BMIM ring to align parallel (concentric) to the electrode surface.

As the curvature of the electrode increases [graphene < (16,16) CNT < (6,6) CNT], the oscillations in the mass density profiles appear to dampen. In particular, the counterion mass density peaks become increasingly smaller and more broadened. The peak (average) density of PF_6 in the first layer is 1.52 (3.23) > 1.43 (3.01) > 1.31 (2.46) g/cm^3 near the positively charged graphene > (16,16) CNT > (6,6) CNT. Similarly near the negatively charged electrodes, the peak (average) density of BMIM in the first layer is 1.15 (3.69) > 1.05 (3.30) > 0.98 (2.62) g/cm^3 for graphene > (16,16) CNT > (6,6) CNT. These observations indicate that the packing density of counterions varies inversely with respect to electrode curvature. In addition, the density of co-ions is also noticeably influenced by the electrode curvature. Near the positively charged electrodes, the first BMIM co-ion peak tends to increase from 0.56 < 0.70 < 0.89 as curvature increases from graphene < (16,16) CNT < (6,6) CNT. Similarly near the negative electrode, the onset of the PF_6 co-ion mass density approaches closer to the electrode surface. Both of these observations are indicative of the fact that the segregation of counterions and co-ions are strongly coupled to, and in fact, diminish with increasing electrode curvature.

The origins of this reduction in ρ_m can depend on a complex combination of factors at the electrode−electrolyte interface. Here, we identify two such factors that may influence the curvature effect on ρ_m: (i) a geometric factor by virtue of the increased volume near curved surfaces and (ii) an electrostatic factor by virtue of the reduced electric field strength near curved surfaces. A detailed discussion of these factors may be found in the Supporting Information. To understand the specific impact of these factors, we further analyzed the space charge variation (ρ_q), mixing parameter (χ), and screening parameter (β).

Figure 3 shows ρ_q in the IL electrolyte near the negatively charged electrodes at $\sigma = -6.3$ and -12.7 $\mu C/cm^2$ (for $\sigma = 6.3$

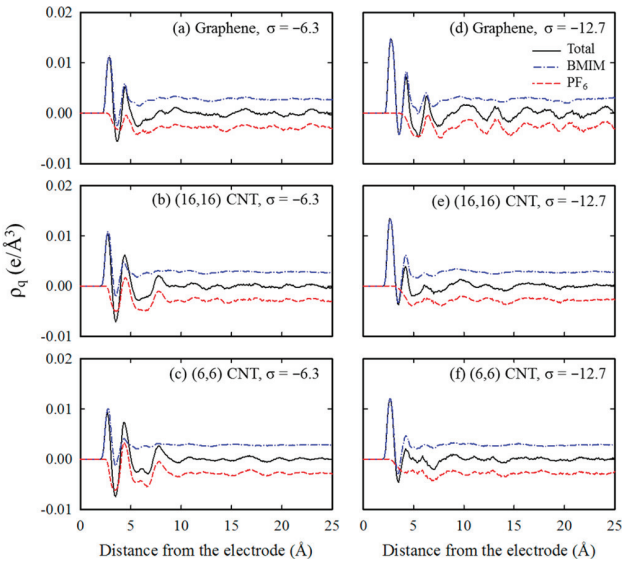

Figure 3. Space charge density profiles (ρ_q) for BMIM, PF_6, and their sum near graphene, (16,16) CNTs, and (6,6) CNTs at the listed σ (in $\mu C/cm^2$) as a function of distance from the electrode surface.

and 12.7 $\mu C/cm^2$, refer to Figure S3); ρ_q was calculated based on the distribution of IL atoms, each with fixed atomic charges. When $\sigma = -6.3$ $\mu C/cm^2$ (a−c), the first peak, which is associated with BMIM (≈ 2.8 Å), has a small tendency to diminish with increasing curvature, deviating from its peak value of 0.011 by only 15%. On the other hand, the first valley, which is associated with PF_6 (≈ 3.6 Å), deepens with increasing curvature; in fact, the minimum value decreases from −0.0056 to −0.0074. This suggests that the ratio of PF_6 co-ions to BMIM counterions in the first layer increases with electrode curvature, which is consistent with the mass density profiles (Figure 2). However, this mixing behavior becomes less apparent when $\sigma = -12.7$ $\mu C/cm^2$ (d−f). In this case, the first BMIM peak is more sensitive to curvature; the peak displays a maximum of 0.015 in the graphene case, which reduces to 0.012 in the (6,6) CNT case. This is indicative of the fact that the BMIM rings, which are planar, can pack more efficiently in a plane than circumferentially. Upon inspection of the PF_6 charge density, we also observe that the onset of the PF_6 contribution has been shifted to 3.8 Å in the graphene case, which increasingly approaches the electrode as curvature increases. This suggests that at $\sigma = -12.7$ $\mu C/cm^2$, the

dx.doi.org/10.1021/jp408085w | J. Phys. Chem. C 2013, 117, 23539−23546

segregation of BMIM from PF_6 is more prominent, although this segregation is less distinct with increased curvature.

To quantify this behavior, we calculated χ (the mixing parameter) as a function of distance from the electrode as shown in Figure 4:

$$\chi = \int_0^z \frac{\rho_{\#,\mathrm{counter}}(z')}{\rho_{\#,\mathrm{counter}}(z') + \rho_{\#,\mathrm{co}}(z')}\,\mathrm{d}z' \tag{1}$$

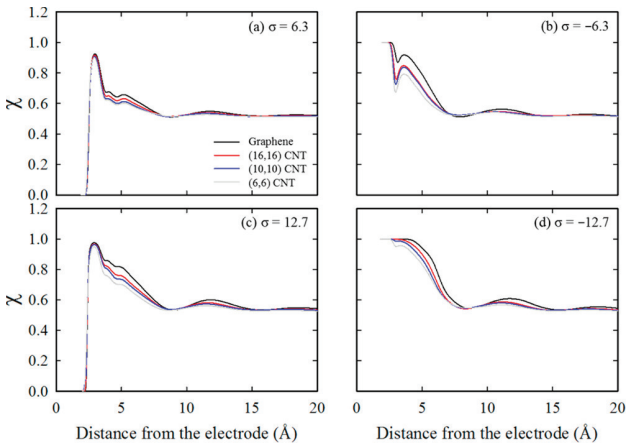

Figure 4. Calculated mixing parameter (χ) with varying electrodes at the listed σ (in $\mu C/cm^2$) as a function of distance from the electrode surface.

where z is the distance from the electrode surface and $\rho_{\#,\mathrm{counter}}$ ($\rho_{\#,\mathrm{co}}$) is the number density of the counterion (co-ion) species. When χ = 0.5, the cumulative number of counterions is perfectly balanced by the number of co-ions; however, by integrating up to the bulk-like region of the finite simulation domain, we expect χ to be slightly larger than 0.5 to account for the net accumulation of counterions in the EDL.

Near the positively charged electrode (Figure 4a,c), the peak ($\approx$ 3.0 Å) value of χ = 0.9 but readily drops toward χ = 0.5. Note, however, that when σ = 6.3 $\mu C/cm^2$, χ tends to decrease more rapidly than when σ = 12.7 $\mu C/cm^2$ (which displays better segregation, i.e., larger χ). The negatively charged electrode (Figure 4b,d) shows a similar trend, suggesting that, in general, the counterions maintain greater segregation from co-ions as σ increases. In fact, the combination of stronger electrostatic attraction (repulsion) between the electrode and counterions (co-ions) as well as the finite space at the interface (limited by so-called lattice saturation) necessitates this behavior; that is, to effectively screen the increasing electric field, counterions will increasingly pack together and contribute to co-ion exclusion.

The influence of electrode curvature on χ seems to strongly depend on both σ and the counterion species. Near the positive electrode at σ = 6.3 (12.7) $\mu C/cm^2$ (Figure 4a,c), the (6,6) CNT case shows a lower χ than the graphene case that deviates by at most 0.06 (0.12). The negative electrode, on the other hand, displays strong sensitivity to curvature when σ = −6.3 $\mu C/cm^2$ (Figure 4b) with χ near the (6,6) CNT deviating by at most 0.19, indicating a noticeable presence of PF_6 co-ions, which is consistent with the charge density profiles (Figure 3f). Interestingly, the curvature dependence of χ is dramatically mitigated when σ = −12.7 $\mu C/cm^2$ (Figure 4d) and shows a sensitivity that is similar to the positive electrode cases.

Figure 5 shows β (the screening parameter) as a function of distance from the electrode, which is an indication of how

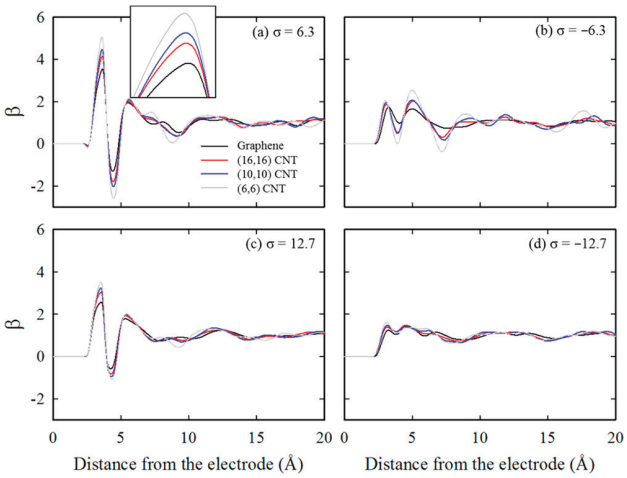

Figure 5. Calculated screening parameter (β) with varying electrodes at the listed σ (in $\mu C/cm^2$) as a function of distance from the electrode surface. The inset in panel a shows the first peak in panel a in greater detail.

effectively the IL screens the electric field (β = 1 indicates perfect screening), and is calculated from

$$\beta = \begin{cases} -\dfrac{\int_R^r \rho_e(r')r'dr'}{\sigma R} & \text{CNT} \\ -\dfrac{\int_0^z \rho_e(z')dz'}{\sigma} & \text{Graphene} \end{cases} \tag{2}$$

where R is the CNT radius.

Our results show that ILs in the EDL typically overscreen the electric field, in good agreement with previous theoretical studies.[30,34,47] In fact, the ions near the positive electrode (Figure 5a,c) generally tend to exhibit stronger overscreening than those near the negative electrodes. This is primarily due to differences in the size and charge distribution of BMIM and PF_6. Near the positive electrode, PF_6 can tightly pack together due to its "spherical" symmetric shape; the first sharp peak (in Figure 5a,c) is attributed to the F atoms, which are modeled here with a partial charge of −0.39 e. By contrast, the positive charge in BMIM is spread somewhat broadly over its ring, which can partially account for the smaller peaks near the negative electrode (Figure 5b,d). The peak is also diminished since BMIM does not accumulate as readily as its PF_6 counterpart due to its bulky structure. As a result, PF_6 seems to be more effective at screening the electric field compared to BMIM. Furthermore, the peaks in β tend to diminish as σ increases since the packing density of ions approach an asymptote that is defined by steric limitations. As σ increases further beyond the so-called lattice saturation limit, the first IL layer is expected to have β < 1.

From Figure 5, we also observe that increasing the electrode curvature results in additional screening by the first IL layer. Note that the larger β near the CNTs is an indication of a greater net number of counterions (i.e., those that are not paired with co-ions) relative to the electrode surface area. This suggests that the counterions prefer to overpopulate the first IL layer due to the increasing availability of space near curved

dx.doi.org/10.1021/jp408085w | J. Phys. Chem. C 2013, 117, 23539−23546

electrodes. Yet despite their larger numbers, these counterions near curved electrodes pack less efficiently in that space as observed from the mass density profiles (Figure 2). This is due to the aforementioned reduced near-surface electric field strength which effectively weakens the ability of the electrode-counterion attraction to overcome the counterion-counterion repulsion. Because of the availability of space, the enhanced screening of the electrode charge by the counterions near the curved electrodes also facilitates the electrostatic attraction between counterions and co-ions, which promotes co-ion mixing at the interface that is consistent with our previous discussion on IL mixing. However, this behavior is also sensitive to the specific ability of the IL counterions to sterically exclude the co-ions as discussed previously.

B. Effect of Curvature on EDL Capacitance. From ρ_q (the charge density), the electric potential (ϕ) profiles along the electrode surface normal direction were calculated by solving Poisson's equation, such that ϕ is given by

$$\phi(z) = \begin{cases} -\frac{\sigma R}{\varepsilon_0}\ln\frac{r}{R} - \frac{1}{\varepsilon_0}\int_R^r \rho_q(r')r'\ln\frac{r}{r'}\,dr' & \text{CNT} \\ -\frac{\sigma z}{\varepsilon_0} - \frac{1}{\varepsilon_0}\int_0^z (z-z')\rho_q(z')\,dz' & \text{Graphene} \end{cases} \quad (3)$$

where ε_0 is the vacuum permittivity.

The calculated potential (ϕ) profiles for graphene and the three CNT cases are shown in Figure 6. In each panel, it is

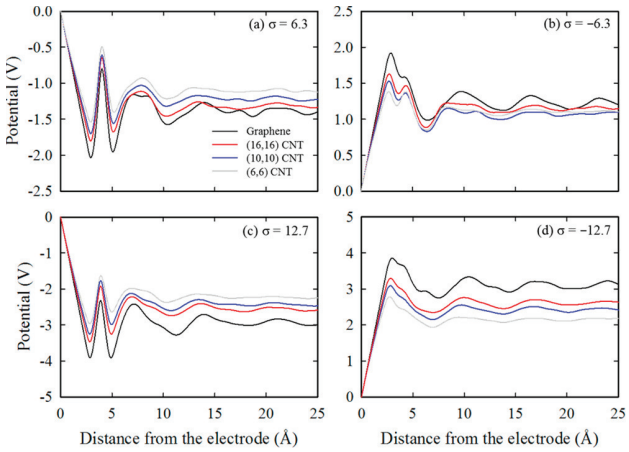

Figure 6. Potential (ϕ) profiles with varying electrodes at the listed σ (in $\mu C/cm^2$) as a function of distance from the electrode surface. The potential is taken in reference to the electrode surface potential.

evident that the $|\phi|$ increases more rapidly near interfaces with decreasing electrode curvature; for instance, the $|\phi|$ in the graphene case at 2.5 Å from the surface is around 0.5 V (1.0 V) more than that of the (6,6) CNT case when $\sigma = \pm 6.3$ (± 12.7) $\mu C/cm^2$. This is primarily attributed to the fact that the electric field strength decays radially in the CNT cases while remaining constant in the graphene case (Figure S1, accordingly from Gauss's law).

Near the positive electrode at $\sigma = 6.3\ \mu C/cm^2$ (Figure 6a), the potential drop across the EDL (ϕ_D = electrode surface potential − the bulk potential) is predicted to range between 1.40 and 1.14 V for the graphene through (6,6) CNT cases, respectively. When $\sigma = 12.7\ \mu C/cm^2$ (Figure 6c), ϕ_D increases and ranges from 2.98 to 2.24 V for the graphene through (6,6) CNT cases. It seems that the differences in ϕ_D are primarily dominated by the deviation in $|\phi|$ in the region between the electrode and IL (due to the aforementioned curvature effect on the electric field strength). On the other hand, as demonstrated earlier (Figure 4a,c), the counterion-co-ion segregation at the electrode−IL interface is minimally influenced by electrode curvature and therefore has little effect on ϕ_D.

Near the negative electrode at $\sigma = -6.3\ \mu C/cm^2$ (Figure 6b), ϕ_D ranges from −1.18 and −1.07 V for the graphene through (6,6) CNT cases, respectively. In contrast to when $\sigma = 6.3\ \mu C/cm^2$, the electrode curvature seems to have a reduced effect on ϕ_D, suggesting that the IL distribution in the EDL, and specifically the counterion-co-ion segregation, causes the curvature effect to be mitigated. This is apparent from the behavior of the potential profiles around 3−4 Å away from the electrode (Figure 6b) which is the location of the first IL layer. As demonstrated by the graphene case, ϕ drops monotonically in highly rich regions of counterions. For each of the CNT cases, ϕ drops then rises as a small hump before dropping again. Recall that when $\sigma = -6.3\ \mu C/cm^2$, the segregation between BMIM and PF_6 is reduced near curved surfaces (Figure 4b), which ultimately lowers the screening of the electric field and increases $|\phi_D|$ for each CNT case such that they are closer to the graphene case. However, the discrepancy in ϕ_D, which ranges from 3.08 to 2.16 for the graphene through (6,6) CNT cases, increases when $\sigma = -12.7\ \mu C/cm^2$ (Figure 6d). Note that the ϕ profiles no longer display a small hump around 3−4 Å away from the electrode, which is consistent with the fact that the curvature effect on χ is greatly mitigated when $\sigma = -12.7\ \mu C/cm^2$ (Figure 4d) due to the increased packing density of BMIM, while PF_6 is also increasingly excluded.

Figure 7 shows the predicted C_D near the positive (a) and negative (b) electrodes with varying curvature, which tends to

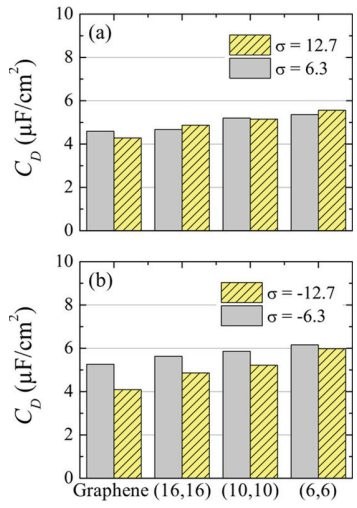

Figure 7. Estimated integral EDL capacitance (C_D) near the labeled (a) positive and (b) negative electrodes with the listed σ (in μ/cm^2).

have a direct linear relationship. Recall that $C_D = \sigma/(\phi_D - \phi_Z)$ where ϕ_Z is the potential at zero charge, which is nearly zero in all cases studied. Hence, C_D increases with curvature as a result of the decreasing ϕ_D. Near the positive electrode, the C_D at each electrode does not change significantly for both $\sigma = 6.3$ and 12.7 $\mu C/cm^2$. This is due to the ability of PF_6 to pack efficiently, thereby preventing lattice saturation. However, we

dx.doi.org/10.1021/jp408085w | J. Phys. Chem. C 2013, 117, 23539−23546

can expect C_D to drop as σ continues to increase. The C_D is also suppressed when σ goes from −6.3 to −12.7 μC/cm^2, which results from the lattice saturation by BMIM. Interestingly, the drop in C_D seems to be increasingly mitigated with electrode curvature; the onset of lattice saturation, as discussed previously, is suppressed near curved surfaces. Curved electrodes, then, can operate at higher ϕ_D before C_D suffers from IL overcrowding effects. However, the specific effect of curvature on C_D can change for different IL pairings; for example, CNT/[EMIM][TFSI] systems were previously predicted to have nearly flat $C_D - \phi_D$ profiles (over a range of −3 to 3 V).[31] Nonetheless, the enhanced capacitance that results from increasing the electrode curvature remains consistent.

C. Effect of Curvature on Quantum Capacitance. The capacitance of low-dimensional materials is known as the quantum capacitance, as first formalized by Luryi.[48] The quantum capacitance of graphene and CNTs is defined as $C_Q = d\sigma/d\phi_E$, where $d\sigma$ and $d\phi_E$ refer to the variations of charge density and local potential, respectively. Provided that the electrochemical potential μ is rigidly shifted by $e\phi_G$,[49] C_Q is given by

$$C_Q = e^2 \int_{-\infty}^{+\infty} D(E) F_T(E - \mu)\, dE \quad (4)$$

where e is the elementary charge, $D(E)$ is the electron density of states (DOS), E is the relative energy with respect to E_F, and F_T $[=(4kT)^{-1}\,\mathrm{sech}^2(E/2kT)]$ is the thermal broadening function. Here, we do not consider charge transfer between [BMIM][PF$_6$] and the electrodes, which has been demonstrated in previous simulations.[50]

The DOS of the metallic CNTs were calculated using DFT, as shown in Figure 8a. Note that the DOS is nearly constant ($\approx$ 0.15 eV^{-1} Å^{-1}) in all three cases when $|E| < |E_{vh}|$, where E_{vh} is the energy at the so-called Van Hove singularity (VHS). The E_{vh} also tends to reduce with increasing CNT radius.

Figure 8(b) shows the estimated C_Q as calculated from eq 4 and the DOS. The C_Q of the CNTs ($C_{Q,CNT}$) tends to decrease with increasing radius in the flat region near the Fermi level, ranging from 9 to 3 μF/cm^2 in the (6,6) to (16,16) cases. The $C_{Q,CNT}$ profile increasingly converges toward the C_Q of graphene ($C_{Q,Gr}$) with increasing curvature, as expected. Here, we should point out that the magnitude of $C_{Q,CNT}$ near the VHS peaks may be underestimated due to numerical errors and can exhibit larger variation.

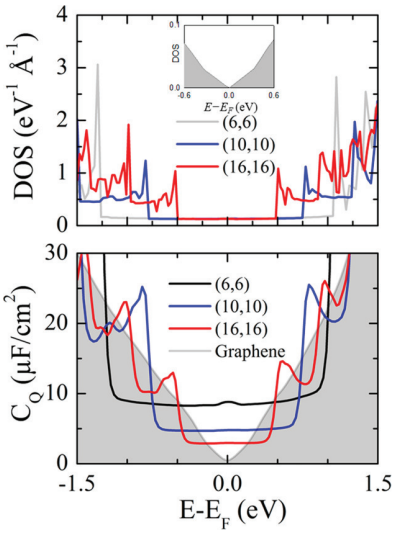

Figure 8. (a) The electronic density of states (DOS) and (b) the calculated quantum capacitance (C_Q) of various electrodes as a function of E. $E = 0$ indicates the position of the Fermi level. The inset of panel a shows the DOS of graphene.

D. Effect of Curvature on Total Interfacial Capacitance. The total capacitance (C_T) at the electrode−IL interface can be represented as a series of C_Q and C_D, i.e., $1/C_T = 1/C_Q + 1/C_D$. With the C_Q and C_D values calculated above, we estimated C_T as a function of applied potential ϕ_a (with respect to the potential of the bulk electrolyte, i.e., $\phi_a = \phi_E + \phi_D$) as shown in Table 1. The relationship between C_Q and C_D with ϕ_a was obtained through σ; recall that $C_Q/C_D \propto \sigma \propto \phi_E/\phi_D$ (Table S2). Note that here we use the integral $C_Q(= \sigma/\phi_E)$.

Table 1. The Estimated Interfacial Capacitance (Applied Potential) for Each Electrode at the Listed Surface Charge Densities σ (in μC/cm^2)

	Graphene	(16,16) CNT	(10,10) CNT	(6,6) CNT
6.3	2.9 (2.2)	2.8 (2.2)	3.0 (2.1)	3.3 (1.9)
−6.3	3.2 (−2.0)	3.2 (−2.0)	3.3 (−1.9)	3.7 (−1.8)
12.7	3.1 (4.2)	3.3 (3.8)	3.5 (3.6)	3.6 (3.5)
−12.7	3.0 (−4.2)	3.4 (−4.0)	3.6 (−3.5)	4.0 (−3.2)

Table 1 shows a summary of the calculated C_T (ϕ_a) for each electrode case when $\sigma = \pm$ 6.3 and $\pm$12.7 μC/cm^2. When $\sigma = \pm$ 6.3 μC/cm^2, C_T tends to be rather insensitive to electrode curvature, and does not increase directly with curvature. In fact, C_T for both the (16,16) and (10,10) CNT cases is predicted to be nearly the same as that of graphene, in contradiction with the trend observed for C_D. This is primarily due to the relatively larger integral C_Q for the graphene case when $\sigma = \pm$ 6.3 μC/cm^2. The values of C_Q for the graphene, (16,16), (10,10), and (6,6) CNTs are around 7.7, 7.3, 7.5, and 9.0 μF/cm^2, respectively; note that the C_Q for the (6,6) CNT is larger because of the VHS. When $\sigma = \pm$ 12.7 μC/cm^2, however, C_T follows the same trend observed for C_D; each of the C_Q values exceeds 10 μF/cm^2 ($\gg C_D = 4$−6 μF/cm^2), making the C_D the dominating factor.

Our study clearly suggests that the influence of electrode curvature on the overall performance is strongly dependent on the relative contributions of C_Q and C_D, which both vary with ϕ_a. Here, we should clarify that the electrode curvature is but one important factor that can influence C_Q and C_D; other modifications to the electrode including impurities, functional groups, and structural defects can also alter C_Q and/or C_D, which should be further investigated. However, we note that additional factors may need to be considered for more quantitative analysis of C_T. For instance, we have neglected the possible polarization of the electrodes[51] and IL ions at the interface and its effect on the electrode charge distribution, the space charge density, and subsequently, C_D. In addition, the DOS (and C_Q) may be altered to a certain extent if the local electronic structure is modified by electrode-IL interactions, which were omitted for simplicity. Nonetheless, our computational approach sufficiently captures the importance of both C_Q and C_D on the performance of CNT-based supercapacitors.

IV. SUMMARY

We investigated the influence of CNT electrode curvature in [BMIM][PF$_6$] IL on the interfacial capacitance (C_T) as a

dx.doi.org/10.1021/jp408085w | J. Phys. Chem. C 2013, 117, 23539−23546

function of applied potential (ϕ_a). Here, C_T is evaluated as the double layer (C_D) and electrode quantum (C_Q) capacitances in series, i.e., $1/C_T = 1/C_D + 1/C_Q$. Using classical MD simulations, we determined the EDL microstructure of [BMIM][PF_6] near each electrode surface at excess surface charge densities σ = 0, ±6.3, and ±12.7 $\mu C/cm^2$. We then calculated the potential variation (ϕ) and C_D. Using DFT, we also estimated C_Q from the electronic DOS of each electrode.

Our analysis of the EDL microstructure reveals that general features near graphene electrodes, such as the multilayering of anions/cations and the IL orientations, are consistent near CNT electrodes. However, increasing the electrode curvature tends to reduce the density of IL counterions closest to the electrode, which we find is a consequence of weakened electrostatic attraction between the electrode and counterions. Despite the reduced density, we also find that increasing the electrode curvature enhances the screening of the electrode charge and promotes counterion-co-ion mixing (i.e., less segregation), although increasing σ abates both of these phenomena.

From the calculation results of ϕ, we observe that the potential drop in the EDL (ϕ_D) diminishes as electrode curvature increases. This reduction is primarily attributed to the fact that the electric field strength decays radially near the CNTs while remaining constant near graphene. When $\sigma = -6.3$ $\mu C/cm^2$, however, the curvature effect is mitigated and is ascribed to the increased mixing of counterions and co-ions near the CNTs; the reduced segregation effectively lowers the screening of the electric field such that ϕ_D is less sensitive to curvature.

The lower ϕ_D amounts to a larger C_D, which tends to increase as electrode curvature increases. When $\sigma = \pm 6.3$ $\mu C/cm^2$, for example, an enhancement of around 18% using (6,6) CNT electrodes is predicted when compared to graphene. As σ increases, we expect C_D to drop due to overcrowding in the EDL, as is observed when $\sigma = -12.7$ $\mu C/cm^2$. Increasing the electrode curvature, however, also increases the available space for IL ions to pack. As a result, the potential window in which C_D does not suffer from lattice saturation effects will be larger near increasingly curved electrodes.

The calculated C_Q for the various CNTs shows a plateau near zero potential with a capacitance that decreases from 9 to 3 $\mu F/cm^2$ as curvature decreases from the (6,6) to (16,16) CNT cases. The potential window of the plateau also diminishes with increased curvature, beyond which C_Q is enhanced as a result of the so-called Van Hove singularities (VHS).

The predicted C_T is demonstrated to vary insignificantly with electrode curvature when $\sigma = \pm 6.3$ $\mu C/cm^2$, in contrast with the predicted trend for C_D. This is primarily due to the influence of C_Q, which varies nonmonotonically with curvature. When $\sigma = \pm 12.7$ $\mu C/cm^2$, however, C_T follows the same trend as C_D; each of the C_Q values exceeds 10 $\mu F/cm^2$ ($\gg C_D = 4-6$ $\mu F/cm^2$), making the C_D the dominating factor. Our analysis therefore suggests that any benefit in C_T due to electrode curvature will in fact strongly depend upon the applied potential.

■ ASSOCIATED CONTENT

Ⓢ Supporting Information

This includes additional simulation details, an in-depth discussion of the geometric and electrostatic factors that contribute to the observed mass density profiles, mass density profiles at $\sigma = \pm 6.3$ $\mu C/cm^2$, charge density profiles near the positive electrode, and a tabulated summary of ϕ_D, C_D, and C_Q. This material is available free of charge via the Internet at http://pubs.acs.org.

■ AUTHOR INFORMATION

Corresponding Author

*E-mail: gshwang@che.utexas.edu.

Author Contributions

†These authors equally contributed to this work.

Notes

The authors declare no competing financial interest.

■ ACKNOWLEDGMENTS

This work was supported by the R.A. Welch foundation (F-1535) and the U.S. Department of Energy, Office of Basic Energy Sciences, Division of Materials Sciences and Engineering (DE-SC001951). We would like to thank the Texas Advanced Computing Center for use of their computing resources.

■ REFERENCES

(1) Wang, G.; Zhang, L.; Zhang, J. A Review of Electrode Materials for Electrochemical Supercapacitors. *Chem. Soc. Rev.* **2012**, *41*, 797−828.

(2) Conway, B. E. *Electrochemical Supercapacitors: Scientific Fundamentals and Technological Applications*; New York: Kluwar Academic, 1999

(3) Lewandowski, A.; Galinski, M. Carbon−Ionic Liquid Double-Layer Capacitors. *J. Phys. Chem. Solids* **2004**, *65*, 281−6.

(4) Simon, P.; Gogotsi, Y. Materials for Electrochemical Capacitors. *Nat. Mater.* **2008**, *7*, 845−54.

(5) Jiang, H.; Lee, P.; Li, C. 3D Carbon Based Nanostructures for Advanced Supercapacitors. *Energy Environ. Sci.* **2012**, *6*, 41−53.

(6) Wang, Y.; Shi, Z.; Huang, Y.; Ma, Y.; Wang, C.; Chen, M.; Chen, Y. Supercapacitor Devices Based on Graphene Materials. *J. Phys. Chem. C* **2009**, *113*, 13103−13107.

(7) Huang, X.; Qi, X.; Boey, F.; Zhang, H. Graphene-Based Composites. *Chem. Soc. Rev.* **2012**, *41*, 666−86.

(8) Rogers, R. D.; Seddon, K. R. Ionic Liquids − Solvents of the Future? *Science* **2003**, *302*, 792−3.

(9) Xu, W.; Angell, C. A. Solvent-Free Electrolytes with Aqueous Solution-Like Conductivities. *Science* **2003**, *302*, 422−5.

(10) Garcia, B. B.; Candelaria, S. L.; Cao, G. Nitrogenated Porous Carbon Electrodes for Supercapacitors. *J. Mater. Sci.* **2012**, *47*, 5996−6004.

(11) Guo, H.; Gao, Q. Boron and Nitrogen Co-Doped Porous Carbon and Its Enhanced Properties as Supercapacitor. *J. Power Sources* **2009**, *186*, 551−556.

(12) Mishra, A. K.; Ramaprabhu, S. Functionalized Graphene Based Nanocomposites for Supercapacitor Applications. *J. Phys. Chem. C* **2011**, *115*, 14006−14013.

(13) Li, Z. J.; Chang, T. X.; Yun, G. Q.; Jia, Y. Coating Single Walled Carbon Nanotube with SnO_2 and Its Electrochemical Properties. *Powder Technol.* **2012**, *224*, 306−310.

(14) Jeong, H. M.; Lee, J. W.; Shin, W. H.; Choi, Y. J.; Shin, H. J.; Kang, J. K.; Choi, J. W. Nitrogen-Doped Graphene for High-Performance Ultracapacitors and the Importance of Nitrogen-Doped Sites at Basal Planes. *Nano Lett.* **2011**, *11*, 2472−77.

(15) Jiang, B.; Tian, C.; Wang, L.; Sun, L.; Chen, C.; Nong, X.; Qiao, Y.; Fu, H. Highly Concentrated, Stable Nitrogen-Doped Graphene for Supercapacitors, Simultaneous Doping and Reduction. *Appl. Surf. Sci.* **2012**, *258*, 3438−43.

(16) Qiu, Y.; Zhang, X.; Yang, S. High Performance Supercapacitors Based on Highly Conductive Nitrogen-Doped Graphene Sheets. *Phys. Chem. Chem. Phys.* **2011**, *13*, 12554−58.

(17) Sun, L.; Wang, L.; Tian, C.; Tan, T.; Xie, Y.; Shi, K.; Li, M.; Fu, H. Nitrogen-Doped Graphene with High Nitrogen Level via a One-Step Hydrothermal Reaction of Graphene Oxide with Urea for Superior Capacitive Energy Storage. *RSC Advances* **2012**, *2*, 4498−506.
(18) Ijima, S. Helican Microtubules of Graphitic Carbon. *Nature* **1991**, *354*, 56−8.
(19) Bandaru, P. R. Electrical Properties and Applications of Carbon Nanotubes Structures. *J. Nanosci. Nanotechnol.* **2007**, *7*, 1−29.
(20) Schnorr, J. M.; Swager, T. M. Emerging Applications of Carbon Nanotubes. *Chem. Mater.* **2011**, *23*, 646−657.
(21) An, K. H.; Kim, W. S.; Park, Y. S.; Choi, Y. C.; Lee, S. M.; Chung, D. C.; Bae, D. J.; Lim, S. C.; Lee, Y. H. Supercapacitors Using Single-Walled Carbon Nanotube Electrodes. *Adv. Mater.* **2001**, *13*, 497−500.
(22) Honda, Y.; Haramoto, T.; Takeshiga, M.; Shiozaki, H.; Kitamura, T.; Yoshikawa, K.; Ishikawa, M. Performance of Electric Double-Layer Capacitor with Vertically Aligned MWCNT Sheet Electrodes Prepared by Transfer Methodology. *J. Electrochem. Soc.* **2008**, *155*, A930−5.
(23) Kaempgen, M.; Chan, C. K.; Ma, J.; Cui, Y.; Gruner, G. Printable Thin Film Supercapacitors Using Single-Walled Carbon Nanotubes. *Nano Lett.* **2009**, *9*, 1872−6.
(24) Lu, W.; Qu, L.; Henry, K.; Dai, L. High Performance Electrochemical Capacitors from Aligned Carbon Nanotube Electrodes and Ionic Liquid Electrolytes. *J. Power Sources* **2009**, *189*, 1270−1277.
(25) Kim, B. W.; Chung, H. G.; Min, B. K.; Kim, H. G.; Kim, W. Electrochemical Capacitors Based on Aligned Carbon Nanotubes Directly Synthesized on Tantalum Substrates. *Bull. Korean Chem. Soc.* **2010**, *31*, 3697−3702.
(26) Huang, J.; Sumpter, B. G.; Meunier, V. A Universal Model for Nanoporous Carbon Supercapacitors Applicable to Diverse Pore Regimes, Carbon Materials, and Electrolytes. *Chem.—Eur. J.* **2008**, *14*, 6614−26.
(27) Shim, Y.; Kim, H. J. Nanoporous Carbon Supercapacitors in an Ionic Liquid: A Computer Simulation Study. *ACS Nano* **2010**, *4*, 2345−55.
(28) Feng, G.; Cummings, P. T. Supercapacitor Capacitance Exhibits Oscillatory Behavior as a Function of Nanopore Size. *J. Phys. Chem. Lett.* **2011**, *2*, 2859−2864.
(29) Huang, J.; Sumpter, B. G.; Meunier, V.; Yushin, G.; Portet, C.; Gogotsi, Y. Curvature Effects in Carbon Nanomaterials: Exohedral versus Endohedral Supercapacitors. *J. Mater. Res.* **2010**, *25*, 1525−31.
(30) Feng, G.; Qiao, R.; Huang, J.; Dai, S.; Sumpter, B. G.; Meunier, V. The Importance of Ion Size and Electrode Curvature on Electrical Double Layers in Ionic Liquids. *Phys. Chem. Chem. Phys.* **2011**, *13*, 1152−61.
(31) Feng, G.; Li, S.; Atchison, J. S.; Presser, V.; Cummings, P. T. Molecular Insights into Carbon Nanotube Supercapacitors: Capacitance Independent of Voltage and Temperature. *J. Phys. Chem. C* **2013**, *117*, 9178−86.
(32) Xia, J.; Chen, F.; Li, J.; Tao, N. Measurement of the Quantum Capacitance of Graphene. *Nat. Nanotechnol.* **2009**, *4*, 505−9.
(33) Stoller, M. D.; Magnuson, C. W.; Zhu, Y.; Murali, S.; Suk, J. W.; Piner, R.; Ruoff, R. S. Interfacial Capacitance of Single Layer Graphene. *Energy Environ. Sci.* **2011**, *4*, 4685−89.
(34) Paek, E.; Pak, A. J.; Hwang, G. S. A Computational Study of the Interfacial Structure and Capacitance of Graphene in [BMIM][PF_6] Ionic Liquid. *J. Electrochem. Soc.* **2013**, *160*, A1−A10.
(35) Paek, E.; Pak, A. J.; Kweon, K. E.; Hwang, G. S. On the Origin of the Enhanced Supercapacitor Performance of Nitrogen-Doped Graphene. *J. Phys. Chem. C* **2013**, *117*, 5610−5616.
(36) Jorgensen, W. L.; Maxwell, D. S.; Tirado-Rives, J. Development and Testing of the OPLS All-Atom Force Field on Conformational Energetics and Properties of Organic Liquids. *J. Am. Chem. Soc.* **1996**, *118*, 11225−36.
(37) Kaminski, G.; Jorgensen, W. L. Performance of the AMBER94, MMFF94, and OPLS-AA Force Fields for Modeling Organic Liquids. *J. Phys. Chem.* **1996**, *100*, 18010−3.
(38) Hoover, W. Canonical Dynamics: Equilibrium Phase-Space Distributions. *Phys. Rev. A* **1985**, *31*, 1695−7.
(39) Plimpton, S. J. Fast Parallel Algorithms for Short-Range Molecular Dynamic. *J. Comput. Phys.* **1995**, *117*, 1−19.
(40) Perdew, J. P.; Wang, Y. Accurate and Simple Analytic Representation of the Electron-Gas Correlation Energy. *Phys. Rev. B* **1992**, *45*, 13244−9.
(41) Kresse, G.; Furthmüller, J. Efficient Iterative Schemes for *Ab Initio* Total-Energy Calculations Using a Plane-Wave Basis Set. J. *Phys. Rev. B* **1996**, *54*, 11169−86.
(42) Blöchl, P. E. Projector Augmented-Wave Method. *Phys. Rev. B* **1994**, *50*, 17953−79.
(43) Monkhorst, H. J.; Pack, J. D. Special Points for Brillouin-Zone Integrations. *Phys. Rev. B* **1976**, *13*, 5188−92.
(44) Wang, S.; Li, S.; Cao, Z.; Yan, T. Molecular Dynamics Simulations of Ionic Liquids at Graphite Surfaces. *J. Phys. Chem. C* **2010**, *114*, 990−5.
(45) Maolin, S.; Fuchun, Z.; Guozhong, W.; Haiping, F.; Chunlei, W.; Shimou, C.; Yi, Z.; Jun, H. Ordering Layers of [BMIM][PF_6] Ionic Liquid on Graphite Surfaces: Molecular Dynamics Simulation. *J. Chem. Phys.* **2008**, *128*, 134504.
(46) Kislenko, S. A.; Samoylov, I. S.; Amirov, R. H. Molecular Dynamics Simulation of the Electrochemical Interface Between a Graphite Surface and the Ionic Liquid [BMIM][PF_6]. *Phys. Chem. Chem. Phys.* **2009**, *11*, 5584−90.
(47) Bazant, M. Z.; Storey, B. D.; Kornyshev, A. A. Double Layer in Ionic Liquids: Overscreening vs. Crowding. *Phys. Rev. Lett.* **2011**, *106*, 046102.
(48) Luryi, S. Quantum Capacitance Devices. *Appl. Phys. Lett.* **1988**, *52*, 501−3.
(49) John, D. L.; Castro, L. C.; Pulfrey, D. L. Quantum Capacitance in Nanoscale Device Modeling. *J. Appl. Phys.* **2004**, *96*, 5180−4.
(50) Ghatee, M. H.; Moosavi, F. Physisorption of Hydrophobic and Hydrophilic 1-Alkyl-3-methylimidazolium Ionic Liquids on the Graphenes. *J. Phys. Chem. C* **2011**, *115*, 5626−36.
(51) Merlet, C.; Péan, C.; Rotenberg, B.; Madden, P. A.; Simon, P.; Salanne, M. Simulating Supercapacitors: Can We Model Electrodes As Constant Charge Surfaces? *J. Phys. Chem. Lett.* **2013**, *4*, 264−8.